PAPER

Check for updates

A highly efficient broadband multi-functional metaplate†

Azhar Javed Satti,‡[b] Muhammad Ashar Naveed,‡[a] Isma Javed,[b] Nasir Mahmood,[b] Muhammad Zubair, [ID][b] Muhammad Qasim Mehmood [ID] *[b] and Yehia Massoud*[b]

Due to the considerable potential of ultra-compact and highly integrated meta-optics, multi-functional metasurfaces have attracted great attention. The mergence of nanoimprinting and holography is one of the fascinating study areas for image display and information masking in meta-devices. However, existing methods rely on layering and enclosing, where many resonators combine various functions effectively at the expense of efficiency, design complication, and complex fabrication. To overcome these limitations, a novel technique for a tri-operational metasurface has been suggested by merging PB phase-based helicity-multiplexing and Malus's law of intensity modulation. To the best of our knowledge, this technique resolves the extreme-mapping issue in a single-sized scheme without increasing the complexity of the nanostructures. For proof of concept, a multi-functional metasurface built of single-sized zinc sulfide (ZnS) nanobricks is developed to demonstrate the viability of simultaneous control of near and far-field operations. The proposed metasurface successfully verifies the implementation of a multi-functional design strategy with conventional single-resonator geometry by reproducing two high-fidelity images in the far field and projecting one nanoimprinting image in the near field. This makes the proposed information multiplexing technique a potential candidate for many high-end and multi-fold optical storage, information-switching, and anti-counterfeiting applications.

1. Introduction

Planar structures with smaller features than the operational wavelength, known as metasurfaces, have demonstrated an amazing ability to govern fundamental properties of incoming light at the subwavelength scale, such as amplitude, polarization, and phase.[1–10] Metasurfaces, with their capacity to accurately control electromagnetic fields, offer a new trail in imaging technology where they may be used to project holographic images or record nanoimprinted images more efficiently with high resolution.[11–14] A one-of-a-kind metasurface that combines holography and nanoimprinting has evolved as an aesthetic approach for data multiplexing and encryption. The key to this approach is the simultaneous modification of the phase and amplitude of the incident light. Numerous approaches have been reported to manipulate the far-field and near-field of the metasurface.[15–18] These far-field holograms, known as Fourier-type holograms, have propagation distances that are significantly greater than the operating wavelength, whereas near-field patterns, known as Fresnel holograms, have propagation distances in the order of a wavelength. To alter the incident light amplitude and phase, different types of nanostructures can be built by segmenting them in the same plane,[19,20] stacking them in many layers,[21] interleaving,[22,23] and phase merging,[24] which have been reported and create additional capabilities for producing picture displays in both the far and near fields. All these approaches have improved the information encoding capabilities but at the cost of efficiency or complex designing. As a result, a light parameter (incident angle, polarization *etc.*) that works for one purpose is essentially noise for another, lowering device efficiency, and crosstalk between functions is obvious.

Many design techniques have been developed by combining holography with nanoimprinting on a single metasurface by adjusting the amplitude and phase of the incoming wave to enhance data encoding capacity.[25–27] For instance, photographic projections for both the near- and far-field may be controlled by adjusting the amplitude and phase of the incoming wave.[25,28] This can be accomplished by stacking patterns on both the front and back faces of a device or by using an interleaving design method. Unfortunately, these measures don't strengthen the efficiency of data encryption. By using coupling between two nanoresonators, Bao *et al.* found a complicated way to change the transmission coefficient that can be used for meta-holography and nano-printing.[12] For a multi-functional meta-surface, Overvig *et al.* used a similar method based on the phase

[a]*Department of Electrical and Computer Engineering, University of Nebraska-Lincoln, Lincoln, NE 68588, USA. E-mail: muhammad.mehmood@kaust.edu.sa*

[b]*Innovative Technologies Laboratories (ITL), King Abdullah University of Science and Technology (KAUST), Saudi Arabia. E-mail: yehia.massoud@kaust.edu.sa*

† Electronic supplementary information (ESI) available. See DOI: https://doi.org/10.1039/d2na00953f

‡ These authors contributed equally.

difference between nanoresonators of varying sizes.[29] However, the intensity of the projected beam (which governs the nano-printed image) restricts the divergence accuracy of the far-field holographic image, which is a major downside for the aforesaid methods. A technique incorporating the propagation phase, the geometric phase, and continuous intensity modulation has been developed to address these efficiency issues.[25] The proposed method utilized a matrix of nanoresonators with varying dimensions and a fixed phase difference between them.[25,30–32] Although the proposed technique solves the efficiency issue, it has significant drawbacks, including broadband response dispersion issues and variable nanoresonator dimensions that need a sophisticated manufacturing procedure and high computational cost. Consequently, it is essential to devise a straightforward strategy to resolve all issues associated with efficiency, effectiveness, and fabrication.

Although, the transmission functionality of metasurfaces is heavily dependent on the optical properties of the composite substance, the substance must possess a significant refractive index along with a lower attenuation coefficient for maximum reliability with very little wave interruption. However, purely metal-based plasmonic metasurfaces have low effectiveness in the visible domain due to high ohmic losses within materials.[33] Furthermore, all dielectric-based metasurfaces bypass these limitations by using materials such as titanium dioxide (TiO_2), gallium phosphide (GaP), and gallium nitride (GaN).[34–36] Still, these smooth surfaces possess a large aspect ratio constraint, which needs costly and sophisticated fabrications. Meanwhile, Naveed *et al.* suggested an a-Si:H made metasurface, which gives high transmission for certain wavelengths, but due to high values of attenuation coefficients, a broadband response may not be achieved.[24,37] Keeping in mind all these materials constraints, here we suggest a low-loss dielectric material platform with very low values of attenuation coefficients for the whole visible regime. As a result, it produces a very high transmission efficiency in the visible band with 50%, 60%, and 89% efficiency at 488, 532, and 633 nm.

In this article, we offer a unique and straightforward design strategy that combines spin-decoupling with intensity modulation in accordance with Malus' rule.[38] We used a single, predetermined-sized ZnS/SiO_2 anisotropic meta-nanoresonator to show information multiplexing across three channels. We modified the nanoresonator's parameters (L and W) to cover the entire visible spectrum. Using only the PB-phase of an asymmetric nanoresonator, we could store three distinctive pieces of information on a single metaplate. Each of the three encoded data bits may be decrypted using a distinct combination of incidence polarization circumstances and optical settings. Under the influence of left-hand circularly polarized (LHCP) light, the suggested metasurface projects an image of a "BICYCLE" in the far-field plane, whereas it projects an image of a "ROCKET" onto the same surface when the incoming beam is right-hand circularly polarized (RHCP) (Fig. 1(a)). Alternatively, a near-field grayscale pattern of the "DIAMOND" image is displayed when linearly polarized light is used alongside an appropriate optical setup (Fig. 1(b)). This approach multiplexes data on the metasurface interface efficiently without increasing the design or computational complexity. The suggested technology can be utilized in various advanced and state-of-the-art anti-counterfeiting, information-hiding, and high-density optical storage systems.

2. Materials and methods

2.1. Workflow for the multi-functional metaplate

In order to accomplish a multi-operational metasurface, Malus' law-based amplitude modulation was merged with Pancharatnam–Berry (PB) phase manipulation, where a single cell of a multi-functional metasurface can encode three independent information channels with independently controllable polarization. Each designed meta element has similar geometry but a distinct orientation angle (θ) which may be used to manipulate the PB phase, which is exactly double the orientation angle ($\psi = 2\theta$). The phase delay between both incident polarization
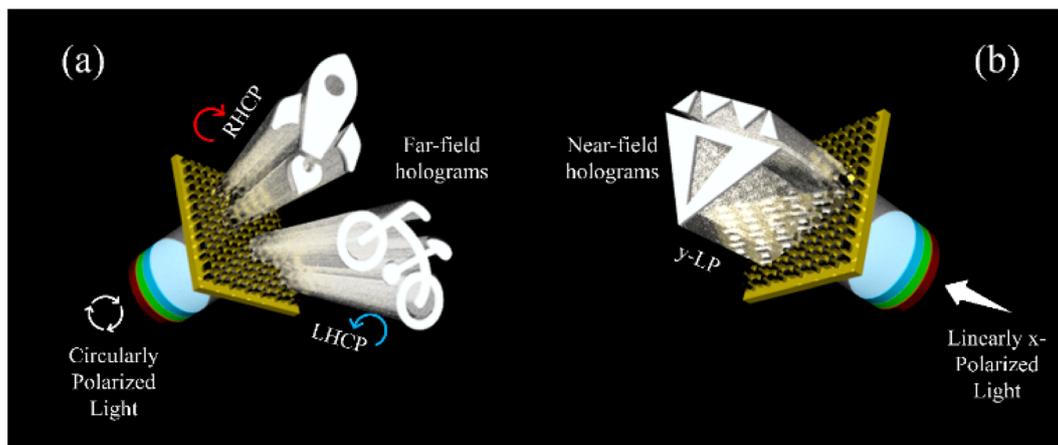

Fig. 1 Demonstration of the suggested idea of a multi-operational metaplate composed of a zinc sulphide (ZnS) nano-resonator over a glass substrate. (a) Under the influence of circularly polarized light, two far field projections are attained, for RHCP incident light the holographic projection of a "ROCKET" is formed while for LHCP incident light the holographic projection of a "BICYCLE" is formed. (b) When linearly *x*-polarized light has shone, the projection of "DIAMOND" will appear in the near field.

directions is always the opposite because the propagation of these incident beams is probably the same as the mirror operation concerning the plane of incident. Thus, a phase delay of -2θ is produced, which gives us the freedom to encrypt separate pieces of information. Furthermore, in this context, we suggested a modified Gerchberg–Saxton (GS) algorithm to numerically evaluate the phase matrices for holographic projections.

First, random phase mapping ${}^{N}_{0}\zeta(x, y)$ is given to evaluate the complex amplitudes for both input objects using the angular spectrum method; the intensity error evaluated afterward is bounded by ε; when this error satisfies the condition, it will give the desired phase, while if not, the inverse Fourier transform is applied to determine a new distribution function by taking the negative of the phase and following a similar procedure to evaluate the final phases $\varphi_{iR}(x, y)$ and $\varphi_{iL}(x, y)$ for metaholograms. Our PB phase manipulation method is based on the fact that orthogonally incident CP light has two consecutive but contrary phase profiles in an anisotropic nanoresonator. This allows for more flexibility in the implementation of spin-decoupling properties. Therefore, two different images can be encrypted and displayed by simply switching the handedness of the incident polarization. The complete PB phase profile of the LHCP and RHCP components of CP light incident from the forward direction on an anisotropic nanoresonator is given by

$$\varphi_m = \arg[\cos\varphi_{iR} + \cos\varphi_{iL} + i(\sin\varphi_{iR} - \sin\varphi_{iL})], \quad (1)$$

where φ_m, φ_{iL}, and φ_{iR} represent the decoupled phase profile and phase profile for LHCP and RHCP incident light,

respectively. By solving eqn (1) to get a full phase profile for two unique information encodings, we obtain[13]

$$\varphi_t = \arg\left[\exp i\left(\tan^{-1}\left[\tan\left(\frac{\varphi_{iL} - \varphi_{iR}}{2}\right)\right]\right)\right]. \quad (2)$$

The two different phases of information that need to be encoded on the metasurface interface are combined into one in eqn (2). Our design method is relatively straightforward and one-of-a-kind in comparison to phase mergence technique-based tri-functional metasurfaces that have been reported previously. These encrypted phase sketches may be decoded by illuminating the CP light to produce two holographic images. When the polarization of the incoming CP light is changed to orthogonal polarization, the projected holographic information switches.

An initial option for capturing the nanoimprinting images is amplitude modulation. The polarization of linearly polarized (LP) light can be altered by passing it through a half-wave plate. So, by rearranging the orientations of the nanoresonator, a metasurface may be utilized to change the intensity of incoming light at the pixel level, allowing for the formation of a continuous grayscale image. Hence, we start with amplitude modulation, for which we've devised an optical configuration including a horizontal polarizer (0°) and an orthogonal polarizer (90°). The emitted intensity of the light "I" when a metasurface is placed in an optical path with orthogonal polarization can be written as[39]
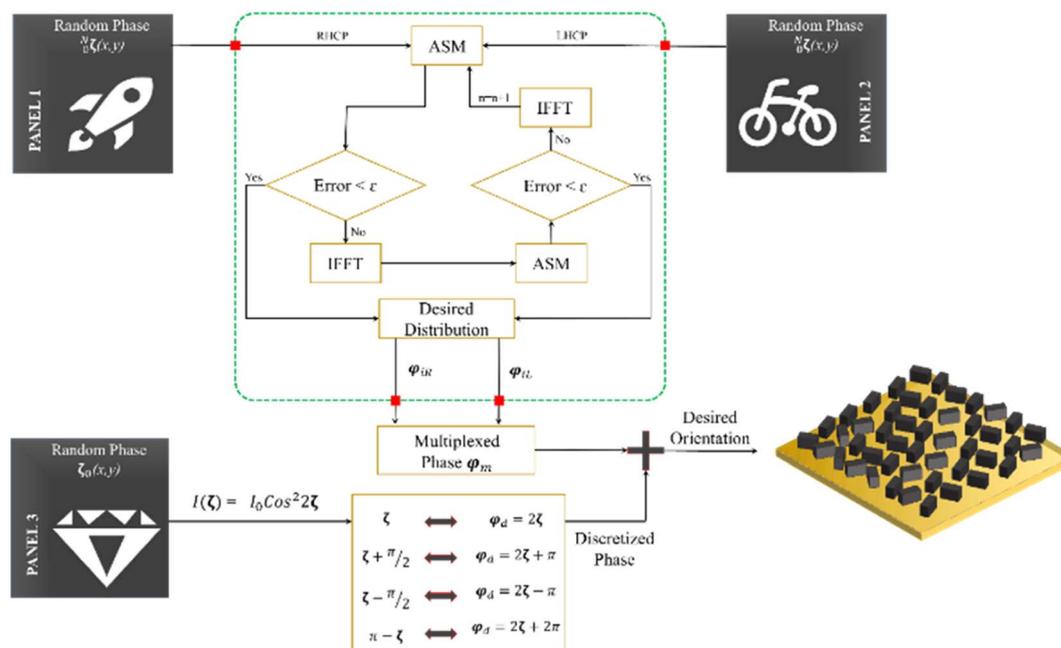
$$I(\zeta) = I_0\cos^2 2\zeta \quad (3)$$

Fig. 2 Design flow model of the multi-functional metaplate. Two random phase patterns are given to determine the complex amplitude using the angular spectrum method; furthermore, by bounding the amplitude error and taking the inverse Fourier transform, we were able to achieve the phase distributions φ_{iL} and φ_{iR} of high-resolution photographs of the "ROCKET" and "BICYCLE." These calculated phases are multiplexed using eqn (2). In addition, we calculated the orientations and approximated the intensity profile of a near-field Fresnel image of "DIAMOND". The proposed trifunctional metasurface is formed by selecting orientations deliberately.

As shown in Fig. 2, due to Malus' law's orientation degeneracy, four different orientation angles can result in the same beam intensity dictated by eqn (3). This "one-to-many mapping" between intensity and rotation gives a new range of options for modifying the PB phase of incoming light. By employing the Pancharatnam–Berry (PB) phase, it is possible to generate a phase delay proportional to twice the nanostructure orientation angle. Each of the four possible orientations results in a distinct PB phase for phase manipulation. As a bonus, we can encode two separate pieces of data in this PB phase manipulation on an individual metaplate by employing the efficient spin decoupling technique.

2.2. Optimization of unit elements

Subwavelength-sized anisotropic meta-nanoresonators locally distort the incident wave's phase and amplitude. Their half-wave plate topology provides great flexibility for implementing spin-decoupling mechanisms with a wide range of helicity requirements. On top of the SiO_2 substrate, we used an array of these identical zinc sulfide (ZnS) nanoresonators with their unique orientations. Consequently, under the influence of circularly polarized light, the transmission efficiency for both cross and co-polarization may be maximized or minimized

accordingly by modifying the physical parameter of the nanoresonator. The maximizing cross-polarized transmission was attained by optimizing the nanoresonator's period (P) via rotation. Considering the Nyquist sampling criterion ($P < \lambda/2NA$, where λ indicates the operating wavelength), we conclude that $P = 410$ nm is the optimal value for the period. In the second step, the long and short faces (W and L) of the nanoresonator are optimized while the period ($P = 410$ nm) and height ($H = 650$ nm) are kept constant. Fig. 3(a–f) demonstrates the obtained cross-polarized transmission efficiencies, whereas the co-polarized efficiency plots are presented in Fig. S1.† Once the criteria for minimum co-polarized and maximum cross-polarized transmission efficiency are met, as they are for the nanoresonator with $W = 260$ nm and $L = 110$ nm, the dimensions satisfying these requirements are highlighted in red. When the chosen nanoresonator is rotated ($0–\pi$) about its axis, the geometric phase associated with anisotropic geometries is activated, allowing full $0–2\pi$ phase coverage. Strong electromagnetic dipole resonances are supported at all operating wavelengths by combining a low extinction coefficient and a high material index. Dipole resonances for $\lambda_3 = 633$ nm are presented in Fig. 3(e and f) and for the other two wavelengths, they are depicted in Fig. S2.†
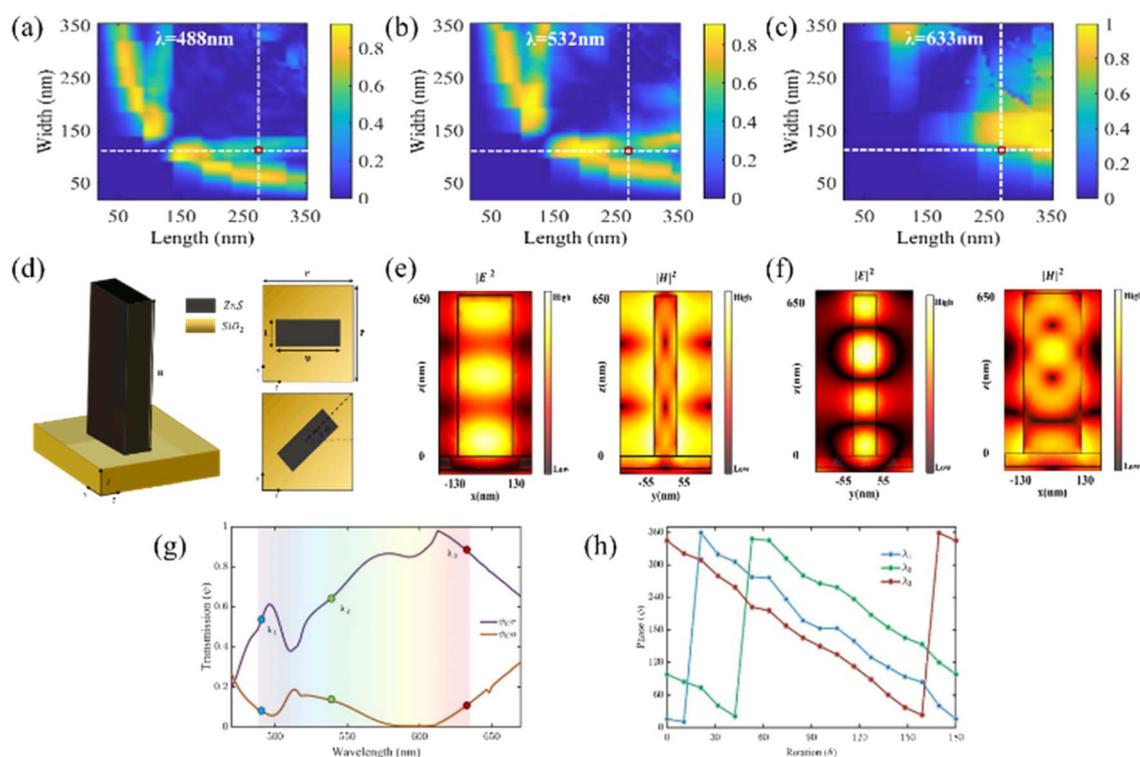
Fig. 3 Broad-band optical functioning was achieved by optimizing the nano-rectangular bar's geometrical properties. (a) Optimization diagrams for the ψ_{cr} of a nanorectangular bar at an optical wavelength of 488 nm, based on the objective function n. ψ_{cr} optimization plots at 532 and 633 nm are presented in (b) and (c), respectively. (d) The optimized dimensions of the nanoresonator are $W = 260$ nm, $L = 110$ nm, and $P = 410$ nm. The asymmetric geometries given by in-plane angular rotation are shown in two plane perspectives. (e) and (f) dissipated an absolute electromagnetic field under x- and y-polarized illumination. The enormous concentration of fields within the nanoresonator allows for high propagation. (g) Transmission of a nano-rectangular bar made of ZnS with tuned L and W. The cross-polarization transmission efficiency of the bar is around 70% throughout practically the visible domain, while the co-polarized transmission is insignificant, *i.e.* <10% across the entire regime. (h) Rotating the bars in the plane produces the $0–2\pi$ phase. Three different wavelengths, $\lambda_1 = 488$ nm, $\lambda_2 = 532$ nm, and $\lambda_3 = 633$ nm, are chosen to ensure full phase coverage and the nano bar's broadband response.

3. Results and discussion

As a proof of concept, we designed and simulated a 100×100 μm^2 metasurface in order to validate our proposed multi-operational metasurface design method. Using high-resolution copies of the "BICYCLE" and "ROCKET" images and the Gerchberg–Saxton (GS) approach, it was possible to determine the whole phase profile for a 243×243 array of far-field unit components. Fig. S3† provides a visual representation of these estimated phase patterns. In order to implement a spin-decoupling approach based on the PB phase, these obtained phase patterns are integrated using eqn (2) to create a multi-mode phase pattern. Also, on a metasurface of size 100×100 μm^2, with pixels measuring 243×243 nm^2, we determined the intensity map of the grayscale "DIAMOND" image. Fig. S3† depicts this computed intensity profile (ESI Section 3†). This computed amplitude profile is then discretized into four orientations (θ, $\pi/2 + \theta$, $\pi/2 - \theta$, and $\pi - \theta$) using eqn (3) to account for Malus' law degeneracy. During metasurface design, the predicted geometric phase profile of the nanoresonator is rounded to the closest viable choices (*i.e.*, θ, $\pi + 2\theta$, $\pi - 2\theta$, and $2\pi - 2\theta$). Therefore, one near-field image and two different far-field images can be encoded on the metaplate with a unique meta-nanoresonator using properly adjusted intensity and phase profiles, respectively (full design flow is given in Fig. 2). Such a designed metaplate is tested using a commercially available finite difference time domain (FDTD) solver. Fig. 4(a1–c3) depicts the simulated outcomes over all three wavelengths

of operation (488, 532, and 633 nm). Under the impact of LHCP incident light, the metaplate produces a far-field projection of a "BICYCLE," while the RHCP incident light produces an image of a "ROCKET" at a focal point 50 μm. When *x*-LP light is incident on the metasurface and examined through a *y*-polarized analyzer within the near-field region, a subwavelength-scale holographic projection of the "DIAMOND" is formed.

Compared to previously reported designing approaches, the suggested single meta-element-based multi-operational meta-plate model has notable technical advantages. For example, using a single nanoresonator (with a constant period, length, width and height) and several precise modulations of the phase and intensity, we could encrypt three unique pieces of information upon that metaplate. The reported studies, however, either contain tricky design methods that render fabrication troublesome or suffer from high crosstalk across shared channels that cannot be removed. Consequently, the proposed design strategy provides a potential choice for high-density optical storage that bypasses these restrictions.

Furthermore, the suggested design method is promising for anti-counterfeiting uses since it requires three separate optical setups to decode three separate bits of information. The near-field information can only be deciphered by using an orthogonally polarized light channel, and far-field information requires varying helicities of incoming CP light. Interpretation of hidden signals in the near field is a big help (not viewable to the naked eye in the distance). To better protect valuable goods from being copied, our suggested metasurface is a great option for a multi-pronged anti-counterfeiting approach.

With a broad response over the visible spectrum, ZnS provides tremendous opportunities in a ZnS/SiO$_2$-compatible technology. Current dielectric platforms, such as gallium phosphide (GaP) and titanium dioxide (TiO$_2$), have challenges owing to their high aspect ratios. However, the suggested material offers almost equivalent performance to existing platforms. In addition, this broadband visible responsive material's integration with electronics sector can open new avenues in chip-integrated panels and wide bandwidth storages.

4. Conclusion

In summary, we show that coupling PB phase modulation with intensity modulation may result in a unique and straightforward design for tri-functional meta-optics. Compared with layering and interleaving design techniques, the recommended strategy leverages a unique nanoresonator to encode many pieces of information on a single metaplate. As a result of a combination of numerous optical feature modifications, the suggested design technique enables a high level of freedom in manipulating individual channels for data encoding. Consequently, the proposed model comprises three independent pieces of information, out of which two are projected on a far-field plane, and one is projected close to the metaplate. Due to its cross-talk-free channels, simple design process, high-resolution findings, and ultra-compact size, the proposed meta-device is appropriate for a variety of high-end applications. Furthermore, the suggested metaplate is suitable for
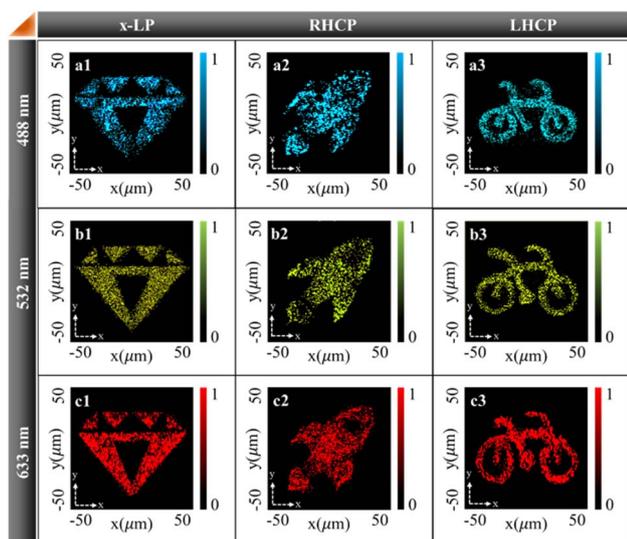
Fig. 4 Simulated outcomes of the tri-operational metaplate. Under the impact of RHCP incident light, a holographic picture of a "ROCKET" is formed in the far field, but with LHCP incident light, a projection of a "BICYCLE" has been generated. On the other hand, the "DIAMOND" image may be seen through a *y*-analyzer in the near field of the metasurface following the impact of *x*-LP incident light. (a1)–(a3) illustrate the incidence for = 488 nm, (b1)–(b3) for = 532 nm, and (c1)–(c3) for = 633 nm. The suggested approach is validated by producing three distinct pictures with high efficiency under various polarization circumstances (RHCP, LHCP, and *x*-LP).

a variety of premium applications owing to its distinctive design and dependable production procedure. Together with the proposed single-step facile fabrication methods, the proposed technique can be valuable for different applications, including high data encapsulation, multi-functional displays, augmented reality, virtual reality, and anti-counterfeiting.[40,41]

Data availability

The data supporting this study's findings are available from the corresponding author upon reasonable request.

Conflicts of interest

There is no conflict of interest to declare by the authors.

Acknowledgements

References

1 H. S. Khaliq, J. Kim, T. Naeem, K. Riaz, T. Badloe, J. Seong, J. Akbar, M. Zubair, M. Q. Mehmood and Y. Massoud, *Adv. Opt. Mater.*, 2022, **10**, 2201175.

2 R. M. H. Bilal, M. A. Saeed, M. A. Naveed, M. Zubair, M. Q. Mehmood and Y. Massoud, *Nanomaterials*, 2022, **12**, 3356.

3 M. A. Naveed, J. Kim, M. A. Ansari, I. Kim, Y. Massoud, J. Kim, D. K. Oh, T. Badloe, J. Lee and Y. Kim, *ACS Appl. Mater. Interfaces*, 2022, **14**, 31194–31202.

4 M. D. Shafqat, N. Mahmood, M. Zubair, M. Q. Mehmood and Y. Massoud, *Nanomaterials*, 2022, **12**, 3285.

5 S. Zakir, R. M. H. Bilal, M. A. Naveed, M. A. Baqir, M. U. A. Khan, M. M. Ali, M. A. Saeed, M. Q. Mehmood and Y. Massoud, *IEEE Photonics J.*, 2022, **15**(1), 1–8.

6 I. Javed, J. Kim, M. A. Naveed, D. K. Oh, D. Jeon, I. Kim, M. Zubair, Y. Massoud, M. Q. Mehmood and J. Rho, *ACS Appl. Mater. Interfaces*, 2022, **14**, 36019–36026.

7 M. Q. Mehmood, J. Seong, M. A. Naveed, J. Kim, M. Zubair, K. Riaz, Y. Massoud and J. Rho, *Adv. Sci.*, 2022, **9**, 2203962.

8 R. M. H. Bilal, S. Zakir, M. A. Naveed, M. Zubair, M. Q. Mehmood and Y. Massoud, *Opt. Mater. Express*, 2023, **13**, 28–40.

9 S. Noureen, M. Q. Mehmood, M. Ali, B. Rehman, M. Zubair and Y. Massoud, *Nanoscale*, 2022, **14**, 16436–16449.

10 S. Ijaz, A. S. Rana, Z. Ahmad, M. Zubair, Y. Massoud and M. Q. Mehmood, *Advanced Devices & Instrumentation*, 2022, 2022.

11 R. Pan, Z. Liu, W. Zhu, S. Du, C. Gu and J. Li, *Adv. Funct. Mater.*, 2021, **31**, 2100689.

12 Y. Bao, Y. Yu, H. Xu, C. Guo, J. Li, S. Sun, Z.-K. Zhou, C.-W. Qiu and X.-H. Wang, *Light: Sci. Appl.*, 2019, **8**, 1–10.

13 M. A. Naveed, J. Kim, I. Javed, M. A. Ansari, J. Seong, Y. Massoud, T. Badloe, I. Kim, K. Riaz and M. Zubair, *Adv. Opt. Mater.*, 2022, 2200196.

14 I. Kim, W.-S. Kim, K. Kim, M. A. Ansari, M. Q. Mehmood, T. Badloe, Y. Kim, J. Gwak, H. Lee and Y.-K. Kim, *Sci. Adv.*, 2021, **7**, eabe9943.

15 M. Wang, G. Hu, S. Chand, M. Cotrufo, Y. Abate, K. Watanabe, T. Taniguchi, G. Grosso, C.-W. Qiu and A. Alù, *eLight*, 2022, **2**, 1–11.

16 W. Wan, J. Gao and X. Yang, *Adv. Opt. Mater.*, 2017, **5**, 1700541.

17 Q. Jiang, G. Jin and L. Cao, *Adv. Opt. Photonics*, 2019, **11**, 518–576.

18 X. Li, X. Zhang, R. Zhao, G. Geng, J. Li, L. Huang and Y. Wang, *Laser Photonics Rev.*, 2022, **16**, 2100592.

19 M. A. Naveed, R. M. H. Bilal, M. A. Baqir, M. M. Bashir, M. M. Ali and A. A. Rahim, *Opt. Express*, 2021, **29**, 42911–42923.

20 A. Shafique, M. A. Naveed, S. Ijaz, M. Zubair, M. Q. Mehmood and Y. Massoud, *Mater. Today Commun.*, 2023, **34**, 105416.

21 B. Yao, X. Zang, Z. Li, L. Chen, J. Xie, Y. Zhu and S. Zhuang, *Photonics Res.*, 2020, **8**, 830–843.

22 J. Kim, D. Jeon, J. Seong, T. Badloe, N. Jeon, G. Kim, J. Kim, S. Baek, J.-L. Lee and J. Rho, *ACS Nano*, 2022, **16**, 3546–3553.

23 M. A. Ansari, I. Kim, D. Lee, M. H. Waseem, M. Zubair, N. Mahmood, T. Badloe, S. Yerci, T. Tauqeer and M. Q. Mehmood, *Laser Photonics Rev.*, 2019, **13**, 1900065.

24 M. A. Naveed, M. A. Ansari, I. Kim, T. Badloe, J. Kim, D. K. Oh, K. Riaz, T. Tauqeer, U. Younis and M. Saleem, *Microsyst. Nanoeng.*, 2021, **7**, 1–9.

25 Z. Li, C. Chen, Z. Guan, J. Tao, S. Chang, Q. Dai, Y. Xiao, Y. Cui, Y. Wang and S. Yu, *Laser Photonics Rev.*, 2020, **14**, 2000032.

26 J. Cheng, Z. Li, D. Y. Choi, S. Yu, W. Liu, H. Wang, Y. Zhang, H. Cheng, J. Tian and S. Chen, *Adv. Opt. Mater.*, 2022, 2202329.

27 A. Overvig and A. Alù, *Laser Photonics Rev.*, 2022, **16**, 2100633.

28 L. Li, H. Zhao, C. Liu, L. Li and T. J. Cui, *eLight*, 2022, **2**, 1–24.

29 A. C. Overvig, S. Shrestha, S. C. Malek, M. Lu, A. Stein, C. Zheng and N. Yu, *Light: Sci. Appl.*, 2019, **8**, 1–12.

30 J. Li, Y. Wang, C. Chen, R. Fu, Z. Zhou, Z. Li, G. Zheng, S. Yu, C. W. Qiu and S. Zhang, *Adv. Mater.*, 2021, **33**, 2007507.

31 Z. Jin, D. Janoschka, J. Deng, L. Ge, P. Dreher, B. Frank, G. Hu, J. Ni, Y. Yang and J. Li, *ELight*, 2021, **1**, 1–11.

32 I. Kim, M. A. Ansari, M. Q. Mehmood, W. S. Kim, J. Jang, M. Zubair, Y. K. Kim and J. Rho, *Adv. Mater.*, 2020, **32**, 2004664.

33 X. Ni, A. V. Kildishev and V. M. Shalaev, *Nat. Commun.*, 2013, **4**, 1–6.

34 S. Sun, Z. Zhou, C. Zhang, Y. Gao, Z. Duan, S. Xiao and Q. Song, *ACS Nano*, 2017, **11**, 4445–4452.

35 B. H. Chen, P. C. Wu, V.-C. Su, Y.-C. Lai, C. H. Chu, I. C. Lee, J.-W. Chen, Y. H. Chen, Y.-C. Lan and C.-H. Kuan, *Nano Lett.*, 2017, **17**, 6345–6352.

36 G. Q. Moretti, E. Cortés, S. A. Maier, A. V. Bragas and G. Grinblat, *Nanophotonics*, 2021, **10**, 4261–4271.

37 N. Mahmood, I. Kim, M. Q. Mehmood, H. Jeong, A. Akbar, D. Lee, M. Saleem, M. Zubair, M. S. Anwar and F. A. Tahir, *Nanoscale*, 2018, **10**, 18323–18330.

38 H. Ren, X. Fang, J. Jang, J. Bürger, J. Rho and S. A. Maier, *Nat. Nanotechnol.*, 2020, **15**, 948–955.

39 S. A. Khan, S. B. Khan, L. U. Khan, A. Farooq, K. Akhtar and A. M. Asiri, in *Handbook of Materials Characterization*, Springer, 2018, pp. 317–344.

40 G. Yoon, K. Kim, D. Huh, H. Lee and J. Rho, *Nat. Commun.*, 2020, **11**, 2268.

41 J. Kim, D. K. Oh, H. Kim, G. Yoon, C. Jung, J. Kim, T. Badloe, H. Kang, S. Kim and Y. Yang, *Laser Photonics Rev.*, 2022, **16**, 2200098.